



Liquid Metal Embrittlement Elimination in RSW of Galvannealed AHSS DP980

Using a new MPEA filler in resistance spot welding of Gen 3 AHSS that preferentially absorbs Zn in solid solution

BY A. ABDELMOTAGALY, B. SCHNEIDERMAN, J. HU, A. CHIH PIN CHUANG, AND Z. YU

Abstract

Liquid metal embrittlement (LME) is a long-standing problem for resistance spot welding (RSW) of Zn-coated automotive sheet steels, especially third generation advanced high-strength steels (AHSSs). This work designed a multi-principal element alloy (MPEA), considered a high entropy alloy (HEA), that preferentially absorbs Zn during RSW and forms a single solid solution phase. The MPEA composition was designed using a high-throughput multi-physics-based analysis, which down-selected the FeMnNiCoZn system as favorable to present a single face-centered cubic (FCC) phase over a broad dilution composition space with the substrate. Comparing the welds made with MPEA foils to control welds without the MPEA, optical microscopy revealed no visible LME cracks in MPEA welds, whereas Zn-lined cracks with a length of 5–100 μm populated the control welds. Energy-dispersive spectroscopy demonstrated the MPEA-limited Zn penetration distance into the AHSS grain boundaries to less than 10 μm . Kinetic simulations also predicted the MPEA would retain Zn as a solid solution and limit its penetration into the AHSS substrate. Site-specific synchrotron diffraction confirmed a single FCC phase in the MPEA and an unaffected ferrite/martensite microstructure in the adjacent DP980 AHSS substrate. Furthermore, tensile-shear tests showed average improvements of 21% in peak load and 80% in fracture energy in welds employing MPEA foils when welded with the same current and schedule.

Keywords

- Liquid Metal Embrittlement
- Resistance Spot Welding
- Galvannealed Advanced High Strength Steel
- Multi-Principal Element Alloy
- High Entropy Alloy

Introduction

Resistance spot welding (RSW) is commonly employed to assemble advanced high-strength steels (AHSSs) for automotive applications (Refs. 1–4). Often, the AHSS is coated with Zn via either galvanizing or galvannealing for improved corrosion resistance. As RSW exerts a thermal profile (Ref. 5) sufficient to locally melt the Zn coating ($T_m = 419.5^\circ\text{C}$), liquid metal embrittlement (LME) may occur under the combined presence of molten Zn and welding-induced tensile stresses. Though LME occurs above the Zn melting point, resultant cracks are retained at room temperature, negatively impacting subsequent mechanical performance (Ref. 3).

LME is acknowledged in the literature as a complex phenomenon influenced by AHSS composition and microstructure alongside welding process variables (Ref. 6). While there has been significant debate in the literature over the relative roles of solid-state diffusion and liquid metal percolation in transporting embrittler atoms along crack propagation pathways (Refs. 3, 7–10), high-angle prior austenite grain boundaries have been generally reported as preferred crack sites (Refs. 6, 7, 11). This lends itself to a degree of LME susceptibility in many AHSS grades regardless of their as-processed microconstituents and to the prevalence of industrial LME concerns in sheet assembly. Galvannealed (GA) steels are usually reported to be less prone to LME than the galvanized (GI) grades, as GA coatings comprise a stabilized Fe-Zn intermetallic compound with a higher melting point than the free Zn employed in GI steels (Refs. 4, 5). However, GA steels are not fully immune to LME.

Several strategies for LME mitigation by manipulating RSW parameters have been investigated in the literature (Refs. 12–15). In one study, increasing the electrode cap size and using round, dome-shaped tips resulted in a 50% reduction in LME crack length in a high-Mn TWIP steel by decreasing the stress applied on the weld periphery (shoulder), yet it did not eliminate the cracks (Ref. 12). Another approach involved using a short precurrent pulse of 10 kA before the primary welding current (12 kA) to remove Zn in situ from the localized weld region before nugget formation (Ref. 13). No cracks were detected via optical evaluation in the welds made by this approach, indicating its potential viability in mitigating LME. However, the base material in this study was 590 MPa TRIP steel, a lower-strength AHSS grade with reduced initial LME susceptibility compared to higher-strength alternatives (Ref. 6). Some studies (Refs. 14, 15) have looked beyond parameter-based means of LME mitigation and employed aluminum foils to dissolve liquid Zn during RSW (Ref. 14) or laser welding (Ref. 15) of Zn-coated steels. Aluminum foils reduced LME significantly in both TRIP 1100 and TRIP 1200 steels by forming iron aluminides that acted as a wetting barrier to molten Zn (Ref. 14). However, in TRIP 1100, an Al-rich LME crack was detected with a trace amount of Zn, raising concerns regarding Al acting as a possible LME agent.

High entropy alloys (HEAs), a novel material class investigated since 2004 (Ref. 16), represent a potential Zn-absorbent material for LME mitigation. HEAs possess several core characteristics, typically comprised of five or more elements in near equiatomic concentrations (Ref. 17), which makes them a promising solution for LME control. Critically, many HEA systems were reported to retain the stability of disordered solid solution phases over a broad composition space due to the high configurational mixing entropy impeding secondary phase formation (Refs. 18, 19). For certain systems, this phase stability extends to multi-principal element alloys (MPEAs), a similar but broader composition space inclusive of both high and “medium” entropy alloys, which may have fewer elements and larger deviations from equiatomic concentrations. This phase stability elevates the potential of these alloys to preferentially accommodate Zn in a stable, ductile solid solution phase with an elevated melting point that cannot act as an LME agent. This study aimed to design an MPEA system to preferentially accommodate Zn in a solid solution and inhibit elemental Zn as an LME agent while avoiding brittle phase formation as it interacts with an AHSS substrate during RSW. This paper first outlines the design approach for the MPEA system. Subsequently, it investigates experimental RSW trials conducted with the designed alloy applied as external foils, including mechanical testing and metallurgical characterization compared to control samples, to study the effectiveness of LME mitigation.

Experimental Methods

MPEA Design

In previous work (Refs. 20, 21), the authors’ research group developed a high-throughput screening strategy for down selection of alloy system candidates using parameter-based filtration. Filtration criteria were based on extended

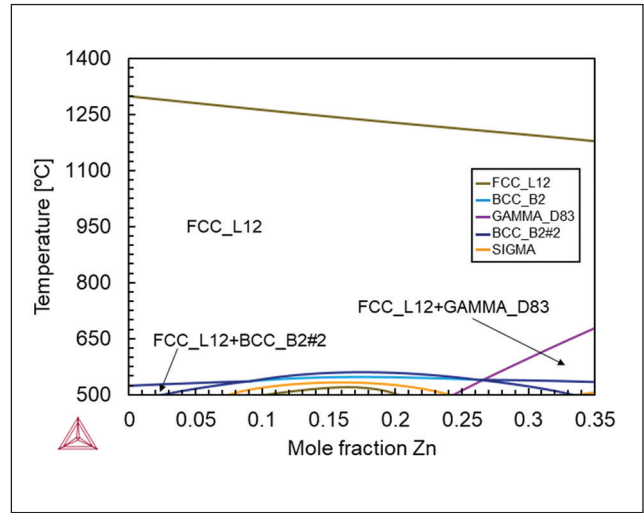


Fig. 1 — Calculated equilibrium phase diagram for FeMnNiCoZn.

Hume-Rothery metrics published in HEA literature (Refs. 16–18, 22–26) targeting a single-phase face-centered cubic (FCC) crystal structure. The four metrics included the atomic size mismatch factor (δ), the valence electron concentration (VEC), the entropy of mixing (ΔS_{mix}), and the enthalpy of mixing (ΔH_{mix}). The governing equations defining these parameters are the following:

$$\delta = \sqrt{\sum_{i=1}^n C_i \left[1 - \frac{r_i}{\bar{r}}\right]^2} \quad (1)$$

$$VEC = \sum_{i=1}^n C_i (VEC)_i \quad (2)$$

$$\Delta S_{mix} = \sum_{i=1}^n -R C_i \ln C_i \quad (3)$$

$$\Delta H_{mix} = \sum_{i=1, i \neq j}^n 4C_i C_j \Delta H_{mix}^{ij} \quad (4)$$

where n is the number of elements; C_i and r_i are the atomic concentration and atomic radius of the element i ; \bar{r} is the average atomic radius of the system’s elements; R is the gas constant; and ΔH_{mix}^{ij} is the binary mixing enthalpy for elements i and j . To target a single-phase FCC crystal structure, the following limits were placed on each criterion: (δ) < 5% (Ref. 24), (VEC) > 8 (Refs. 25, 26), ΔS_{mix} > 12 J/mol. K (Ref. 25), and -15 kJ/mol < ΔH_{mix} < 5 kJ/mol (Ref. 27). The input data for binary enthalpy of mixing, VEC, and atomic radius were obtained from studies by Takeuchi and Inoue (Refs. 22, 28),

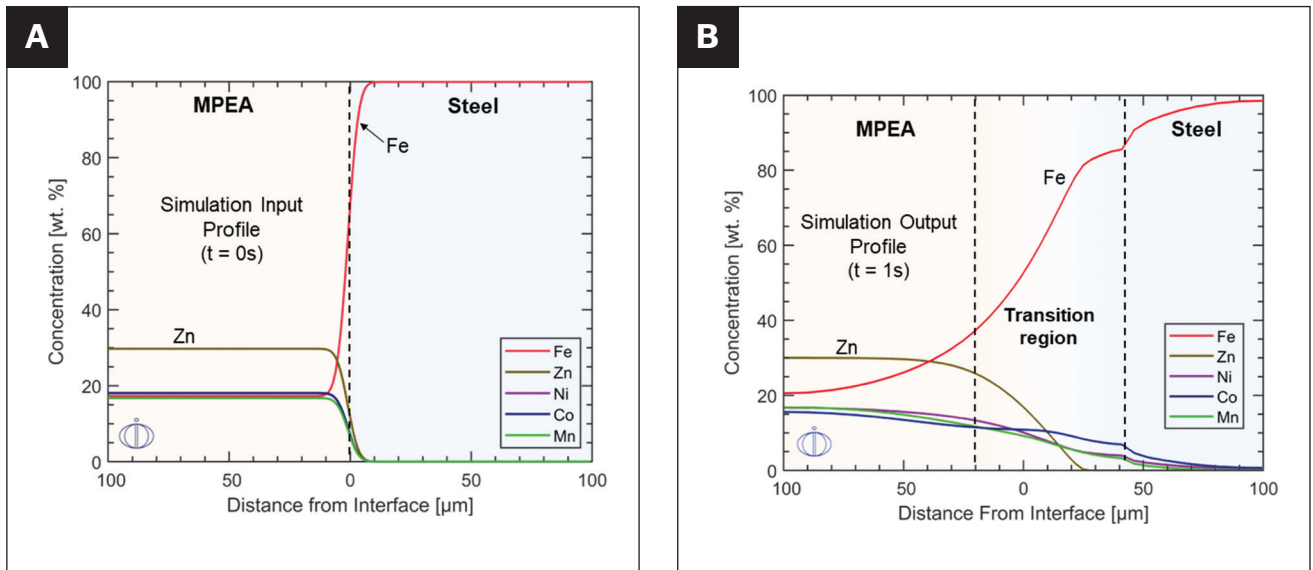


Fig. 2 – A – Initial composition profile input to DICTRA diffusion simulation between FeMnNiCoZn and AHSS substrate; B – resultant composition profile after the DICTRA simulation with a thermal profile modeling a typical RSW process.

Boer (Ref. 29), and Miracle (Ref. 18), respectively. Candidate systems were required to include both Fe and Zn, as they were the prevalent elements in the base material and coating layer. Therefore, they were expected to dilute the MPEA composition during welding. In this initial screening step, the system predicted to retain an FCC solid solution crystal structure over the largest range of Zn concentrations was the FeMnNiCoZn system as patented in Ref. 30, which was further investigated via thermodynamic and kinetic simulations.

Figure 1 displays an equilibrium isopleth phase diagram of the FeMnNiCoZn system, in which the Zn content increases at the expense of the other four elements as their ratios remain fixed and equiatomic. This phase diagram shows the dominance of a single FCC phase at temperatures above 650°C over a Zn concentration range from 0 to 35 at.-%. Other equilibrium phases, including σ , a γ -brass structure, and two BCC phases, are predicted at temperatures below 650°C. The low-temperature stability of these phases in the equilibrium phase diagram did not disqualify this as a candidate system. Given the typically short duration (e.g., 300 to 600 ms of welding time) at elevated temperatures during the RSW process, it was hypothesized that the final welded microstructure would be far from equilibrium and the low-temperature equilibrium phases would not form in appreciable quantities during rapid cooling. More importantly, Fig. 1 indicates the system has a high solubility for Zn at higher temperatures. Therefore, substantial Zn introduction from the coating layer during welding can be tolerated while retaining single-phase stability.

Gibbs free energy calculations using Thermo-Calc software consistently show 10–15 kJ/mol lower free energy overall temperatures below 1000°C when Zn is dissolved in an MPEA solid solution rather than bound in Fe-Zn intermetallic phases. Therefore, in the following kinetics calculations, it is assumed that the MPEA foil will completely absorb Zn coating covering the spot weld during the early heating stage of RSW. This

simplification was made in the diffusion-controlled transport (DICTRA) simulations to avoid the convergence issues faced by a model with three distinct initial regions, including the MPEA foil, Zn coating layer, and semi-infinite ferrous substrate. In this simplified simulation, the initial input was directly modeled as a Zn-infused MPEA adjacent to a steel substrate with a differentiable profile at the interface, as illustrated in Fig. 2A. The MPEA's propensity to retain Zn in a solid solution was evaluated through the DICTRA simulation during the later heating stage to higher temperatures and the cooling stage of RSW. The later experimental work validated this assumption by showing that Zn was preferentially absorbed by the MPEA foil rather than by the AHSS. The Zn concentration was approximately 30 wt-% based on the known coating density of 40–60 gm/m² for GA DP980. The AHSS substrate region was modeled as pure Fe because actual alloying additions to the AHSS are dilute relative to the concentrations in the MPEA. A reported RSW thermal profile (Ref. 31) with a total duration of 1 s and a peak temperature of 2100°C was input to the kinetic simulation.

Figure 2B shows the DICTRA simulation result. Among the MPEA constituents, Zn was predicted to diffuse the shortest distance across the original steel/MPEA interface, 25 μm relative to the original interface boundary, despite having the highest original concentration gradient (i.e., driving force for diffusion) across the boundary. Limited Zn diffusion into the transition region indicated the ability of the MPEA to retain Zn absorbed from the coating. Among the other elements, Co diffused furthest into steel, followed by Ni and Mn. A Fe-dominant transition region rich in MPEA constituents, marked in Fig. 2B, was predicted to extend 40 μm into the steel side of the original interface. The smooth composition curves indicated the formation of a diluted MPEA microstructure without secondary phases in this transition zone. A sudden drop in composition profiles of all MPEA constituent elements, including Zn, beyond this transition region indicated

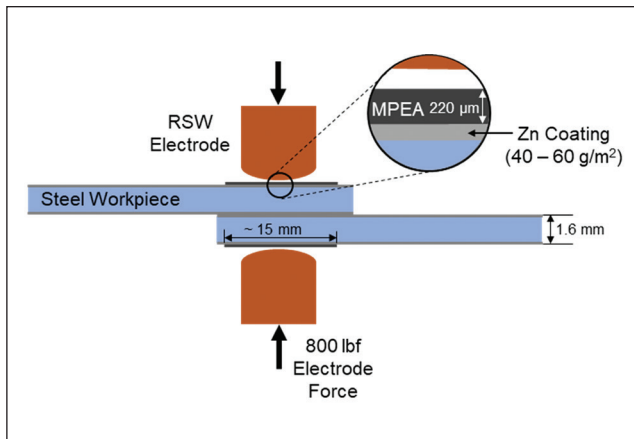


Fig. 3 – Schematic welding setup for RSW samples with two MPEA foils.

a transition to the minimally impacted substrate AHSS. It is noted that the diffusion simulation did not consider grain boundaries, which would heavily influence Zn penetration; however, the result indicated the ability of the MPEA to stabilize Zn in a solid solution in the transition region when in a continuum with the steel substrate, reducing the risk of penetration along grain boundaries.

MPEA Fabrication and Characterization

Ten-gram ingots of the $\text{Fe}_{25}\text{Mn}_{25}\text{Ni}_{25}\text{Co}_{25}$ MPEA were fabricated by arc-melting small solid pieces of the constituent elements with a minimum purity of 99.9%. The quaternary MPEA excluding Zn was produced for experimental trials to maximize the MPEA's capacity to absorb extrinsically introduced Zn from the GA coating layer. Arc-melting employed a gas-tungsten arc welding (GTAW) electrode as the heat source, affixed above a water-cooled copper hearth inside a controlled atmosphere chamber. The chamber was evacuated to approximately 900 millitorr and purged with ultra-high purity argon three times before melting. The GTAW voltage and current were fixed at 220 V and 200 A, respectively. The bulk composition of the as-fabricated MPEA was analyzed by x-ray fluorescence (XRF). The as-cast MPEA ingots were cut into 0.8–1.3-mm-thick sections and cold rolled down to 400–600 μm thickness. The foils were ground using silicon carbide abrasive paper to reach a final thickness of 220 μm . To study the as-cast MPEA microstructure, a sample extracted from the MPEA ingot was ground and polished to a 1 μm diamond suspension step followed by ultrasonic cleaning. Then it was etched for 45 s using 1% nital solution (1 vol-% nitric acid + 99 vol-% methanol).

Welding Procedure

RSW samples joining two coupons of 1.6 mm-thick GA DP980 AHSS were produced with and without the MPEA foils. A commercial galvanized DP980 steel sheet was selected for the study with a chemical composition (wt-%) of Fe-2.23Mn-0.36Mo-0.23Cr-0.11C-0.05Al-0.001Ti-0.001V

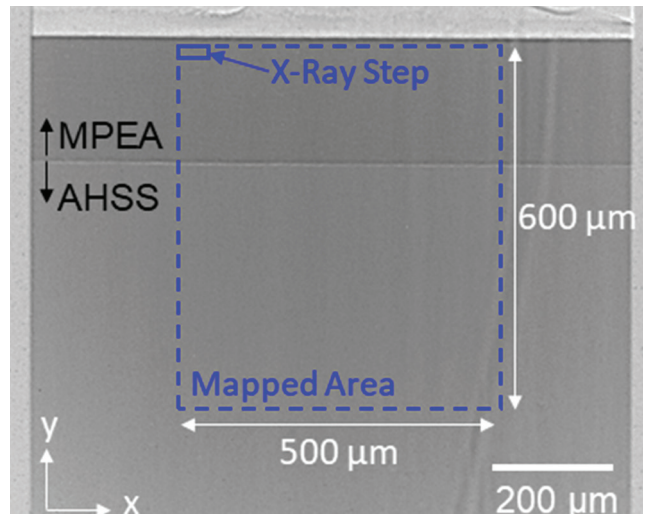


Fig. 4 – Synchrotron x-ray radiographic image illustrating diffraction data collection across the MPEA/steel material interface.

with maximum allowable S and P of 0.012 wt-%, and the Zn-based coating density was 45g/m².

All RSW samples were welded in a lap joint configuration with the spot weld located at the center of the overlapping area (Fig. 3). Samples produced without MPEA foils were denoted as control welds. For samples produced with MPEA foils, Fig. 3 illustrates how two foils were applied on the exterior surfaces of the spot weld between the electrode and the steel sheet. This location was selected to study LME mitigation because the exterior periphery of the RSW electrode indentation (weld shoulders) has been observed to exhibit some of the highest susceptibility to LME cracks (Ref. 3). Foils were gripped with pliers until the RSW electrode force was applied just before welding, after which the pressure of the electrodes was sufficient to hold the foils in place in contact with the AHSS workpiece, and no adhesion aid or additional fixtures were required to fix them.

All samples were welded with constant parameters of 9.5 kA current, 26 cycles (433 ms) time, and 800 lbf load using a 60 Hz RSW machine and a 6.35-mm diameter dome-shaped electrode. These parameters were selected because they were found to produce control samples with ample LME cracks. As such, the effectiveness of MPEA foils on LME control could be readily evaluated. Adding the two foils was expected to increase the welding heat input in the experiment samples, as the foils would increase the total sample electrical resistance. However, for the initial validation of LME control, the welding current was kept constant in both the experimental and control samples. The effect of adding the foils on the generated nugget size will be characterized and discussed later.

Metallurgical Characterization and Mechanical Testing

Optical microscopy investigated the presence of LME cracks in cross sections of welded samples. An FEI Quanta

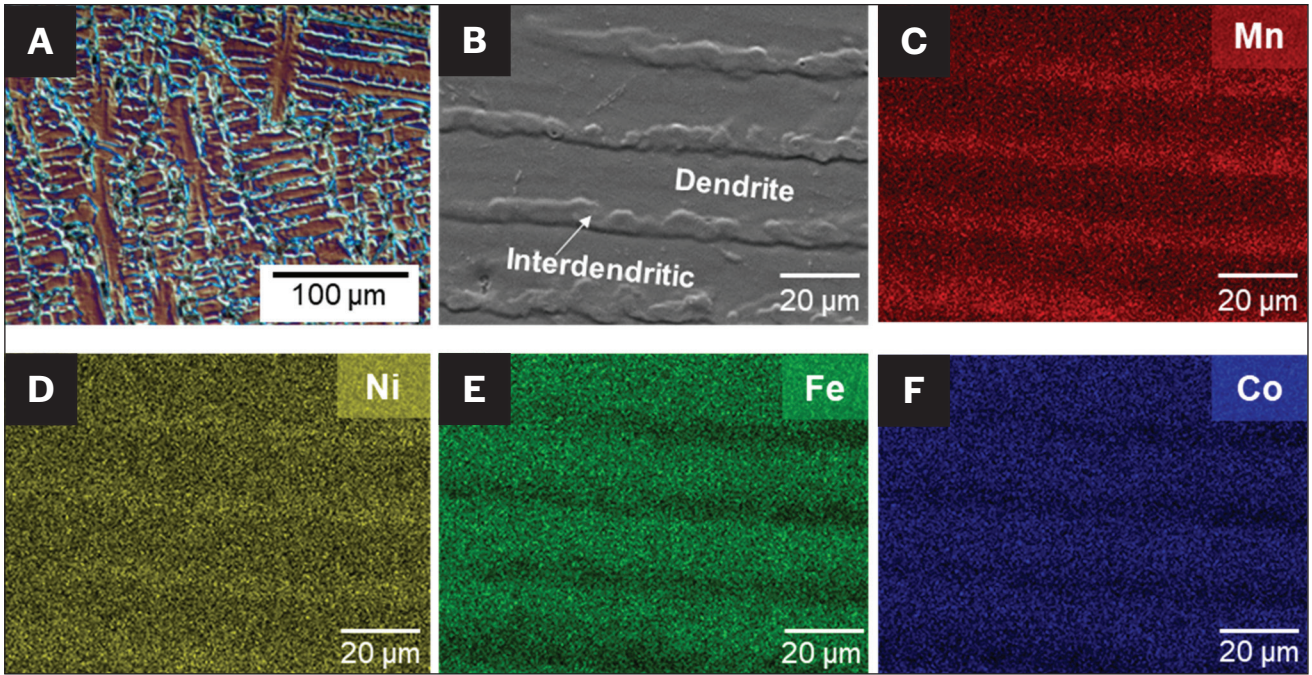


Fig. 5 – Microstructure of the as-cast FeMnNiCo MPEA: A – Polarized light optical micrograph at a low magnification; B – SEM image at a high magnification; C–F – EDS elemental maps for the four constituent elements of the MPEA.

Table 1 – As-Designed vs. As-Cast Chemical Composition of the MPEA

Element (at.-%)	Fe	Mn	Ni	Co
As Designed	25	25	25	25
As Cast (XRF)	24.85	24.12	26.27	24.71

600 environmental scanning electron microscope with energy dispersive spectroscopy (EDS) was used for composition mapping in the as-cast MPEA. Higher resolution imaging and mapping were performed with a JEOL 7000F field-emission scanning electron microscope to investigate the composition profile and Zn penetration in the RSW samples. An accelerating voltage of 20 kV was used in both cases.

Site-specific synchrotron x-ray diffraction (XRD) mapping was performed at Beamline 1-ID-E of the Advanced Photon Source, Argonne National Laboratory, using a setup similar to that described with details in Ref. 32 to assess the constituent phases in the MPEA foil and AHSS substrate regions after RSW. A 1-mm-thick section was cut from the center of an RSW sample using a slow-speed saw with a diamond blade. A monochromatic beam with an energy of 61.332 keV and incident beam size of 30 × 50 μm was directed in transmission through this sample, and a PILATUS3 X CdTe 2M hybrid photon counting detector with a sample-to-detector distance of 740 mm was used to collect diffraction patterns. As illustrated in Fig. 4, the x-ray

beam was raster-scanned over a 500 × 600 μm region with step sizes of 50 μm in the x-direction (lateral) and 20 μm in the y-direction (transverse to the MPEA/steel material interface) to map the constituent crystal structures in this region. Note that although a 20 μm step size was used in the y-direction, the focused beam resolution was limited to approximately 50 μm. Patterns were integrated into one-dimensional data with the Fit2D software calibrated with a cerium dioxide standard. Then, each row of patterns at the same y-position was averaged only across the x-direction. Radiographic reference images such as Fig. 4 were collected with a PointGrey detector with camera model Gs3-u3-23s6m-c with a 2 mm × 1 mm field of view.

Tensile shear testing in the lap joint configuration was conducted on an MTS Alliance RT/100 load frame with a displacement rate of 3 mm/min to compare the RSW load-bearing capacity with and without MPEA foils. Three duplicate samples were tested for each condition. Using image analysis software, stereoscope images of the failed samples were analyzed to estimate the nugget size by tracing the previously bonded region's perimeter.

Results and Discussion

Metallurgical Characterization of the As-Cast MPEA

Table 1 compares the chemical compositions of the as-designed and as-cast MPEA ingot sample measured by XRF.

The polarized light optical micrograph in Fig. 5A displays a dendritic microstructure in the as-cast FeMnNiCo MPEA.

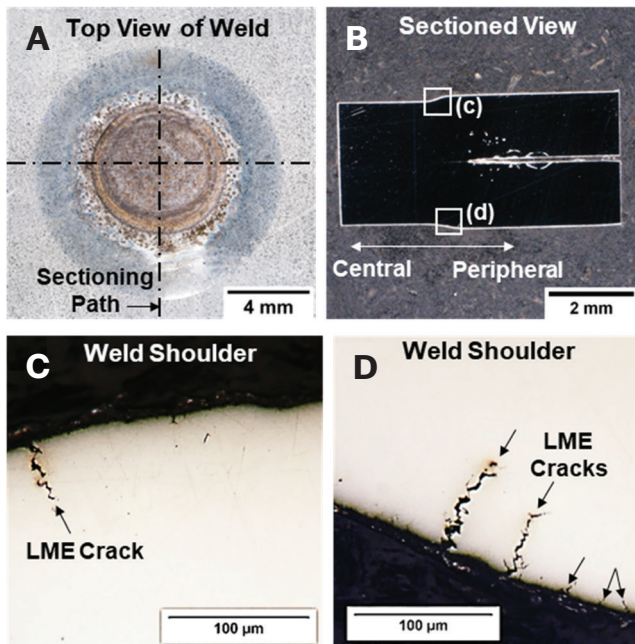


Fig. 6 – Optical macrographs of a control sample without MPEA foils: A – The uncut top view of the weld; B – side view of a cross section along the pathway indicated in A; C–D – two higher-magnification micrographs taken at weld shoulders.

The EDS mapping results in Figs. 5B–F demonstrate segregation of Fe and Co in the dendrites and Mn with a lower melting point segregating to the interdendritic region. A slight segregation of Ni into the interdendritic region was also observed. Similar segregation has been observed in other as-cast MPEA systems and can often be eliminated with a homogenization heat treatment (Ref. 33); however, homogenization of the MPEA was determined to be non-critical to its function as an LME mitigant.

Metallurgical Characterization of the Control RSW Samples

RSW samples were cut into four quadrants, as shown in Fig. 6A, to examine weld cross sections for LME cracks. The optical micrographs of the control weld sample shown in Figs. 6C and D show LME cracks at the peripheral edge of the electrode indentation on the steel sheets (i.e., weld shoulders). LME cracks found in this location are the most common type (Refs. 3, 4). Multiple cracks were observed around the weld shoulders in all the inspected cross sections with a crack length range of 5–100 μm.

Figure 6D shows larger cracks with a maximum width of 10 μm and lengths approaching 100 μm. The EDS maps in Fig. 7 demonstrate the enrichment of Zn throughout the length of these cracks. The quantified EDS line scan data at a surface depth of 45 μm in Fig. 6B indicates that the maximum Zn concentration inside the crack was as high as 50 wt-%. The enrichment of Zn throughout the crack confirmed Zn penetration as the root cause of cracking at

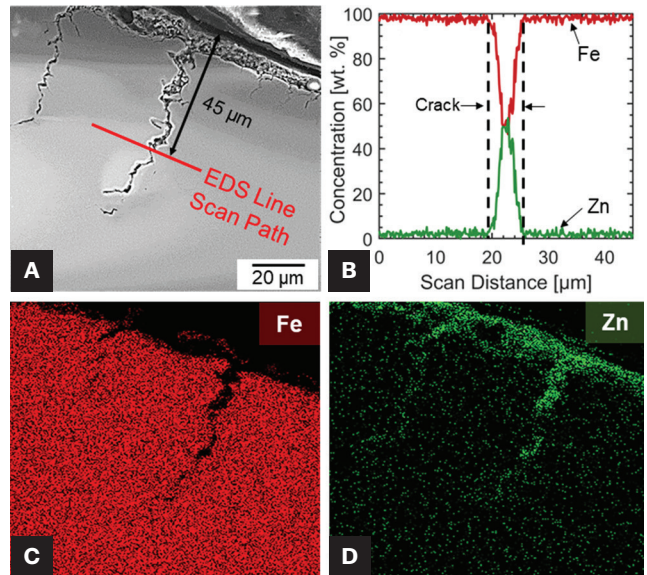


Fig. 7 – A – SEM image corresponding to Fig. 6D; B – EDS line scan Fe and Zn concentration profiles across the crack. EDS map scans of: C – Fe; D – Zn, respectively.

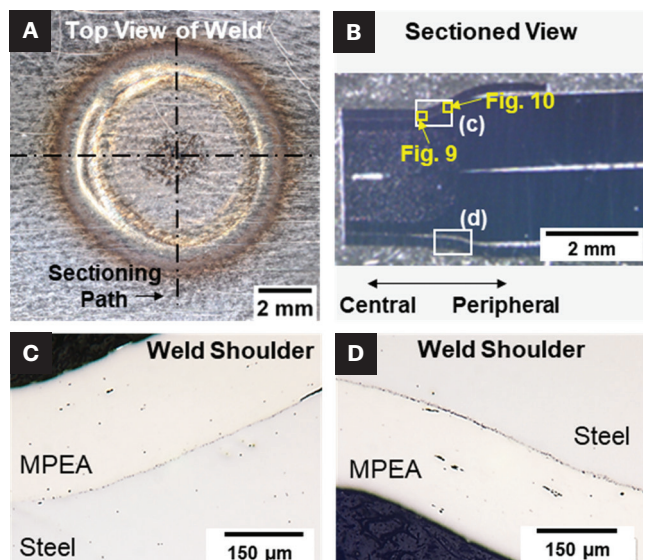


Fig. 8 – Optical macrographs of an RSW sample with MPEA foils applied on exterior surfaces: A – The uncut top view of the weld; B – side view of a cross section of the sample along the pathway indicated in A; C–D – higher-magnification micrographs taken at the weld shoulders.

the shoulders of these conventional welds, confirming LME as the cracking mechanism.

Metallurgical Characterization of the RSW Samples with MPEA Foils

Figure 8 shows typical optical macrographs of the weld sample with MPEA foils. LME cracks are absent at the weld

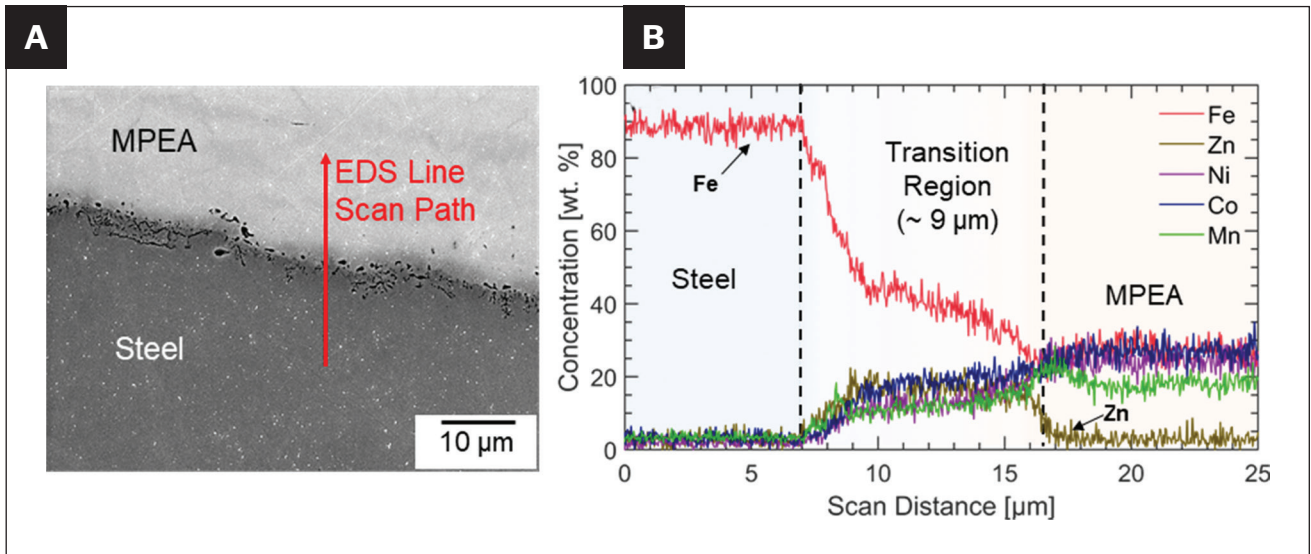


Fig. 9 – A – SEM micrograph; B – EDS line scan data at the MPEA/steel interface in the more central part of the weld shoulder (location indicated in Fig. 8B).

shoulders, an initial indication that the MPEA functioned as an LME mitigant. For further characterization, Fig. 9 shows an SEM micrograph and the EDS composition profile across the MPEA/steel interface in the more central part of the weld shoulder region (see location in Fig. 8B). Figure 9 illustrates a narrow transition region of about 9 μm wide between the AHSS and the MPEA foil, in which the initial composition of the MPEA was enriched with Fe and Zn. The average Zn concentration within this transition region was 18 wt.-%. The similar concentration of Zn to Co, Ni, and Mn across the transition region shows that the Zn concentration correlated with the other elements in the MPEA. This observation indicates that the MPEA incorporated Zn from the coating layer, inhibiting free Zn from penetrating the AHSS substrate, as indicated by the near-zero Zn concentration in the steel base material in Fig. 9B. Moreover, there is no indication of significant diffusion of the other MPEA elements into the steel; the compositionally impacted zone of the steel is smaller than predicted by the DICTRA simulation results in Fig. 2B. The low Zn concentration and near-equiatomic proportions of Mn, Fe, Co, and Ni in the rightmost region of Fig. 9B highlight that only the innermost 9 μm of the MPEA was affected by Zn, meaning that a much smaller amount of MPEA than the 220 μm-thick foil could likely be sufficient for LME mitigation.

Figure 10 shows an SEM micrograph and EDS maps at a more peripheral location of the weld shoulder (location indicated in Fig. 8B). This area exhibits a more pronounced transition region approximately 25–30 μm thick, as seen in the EDS maps. This was likely caused by the electrodes pushing out the molten Zn from the center of the weld indentation and accumulating it at the weld periphery (Ref. 34). Zn was also found to be preferentially absorbed by the MPEA rather than penetrating the steel substrate. A small instance of Zn penetrated the steel grain boundary shorter than 10 μm was observed, as labeled in the Zn map in Fig. 10F. It suggests that the MPEA foil did not completely inhibit Zn penetrating steel grain boundaries but suppressed it to a degree to sufficiently

eliminate the formation of LME cracks. The elimination of LME cracking in welds with MPEA foils is especially noteworthy because adding the foils was expected to increase the weld heat input, which could raise LME susceptibility if Zn penetration into the steel substrate is not mitigated.

Figure 11 presents two synchrotron x-ray diffraction patterns from either side of the MPEA/steel interface, with the locations indicated in the radiographic reference images in the insets. Note that the transition region shown in Figs. 9 and 10, ranging from 9–30 μm, were too narrow to examine in isolation with the ~50 μm spatial resolution in the x-ray beam. Instead, Fig. 11A shows a pattern of a location centered at 60 μm on the MPEA side of the MPEA/steel interface, and Fig. 11B shows a location centered at 60 μm on the steel side. Fig. 11A displays an FCC solid solution as the sole phase present, based on parameter-based filtration predictions and the thermodynamic and kinetic simulations in Figs. 1 and 2. The lattice parameter of the MPEA FCC phase was determined to be 3.598 Å via a peak fitting process described in detail in Ref. 35. While the lattice parameters of MPEA solid solutions vary substantially with composition, this value is similar to that predicted by the statistical hard sphere model discussed in Ref. 36. The entire MPEA region exhibited patterns exemplified by Fig. 11A until the center of the focused beam moved toward 40 μm from the MPEA/steel interface. In this near-interfacial zone, a mixed steel/MPEA diffraction pattern was exhibited due to the beam's 50 μm spatial resolution and possible slight angling of the sample. On the steel side of the interface, Fig. 11B shows strong BCC/BCT peaks corresponding to the primarily ferrite/martensite microstructure characteristic of DP980 AHSS (Refs. 37, 38). Since the tetragonality ratio c/a of martensite was close to Ref. 39, the BCT peaks were nearly indistinguishable from the BCC peaks, but peak broadening existed. As displayed in Fig. 11B, a small fraction of retained austenite was also present. The lattice parameters were 2.867 Å for the ferrite/martensite peaks and 3.596 Å for the retained austenite peaks. These lattice parameters did

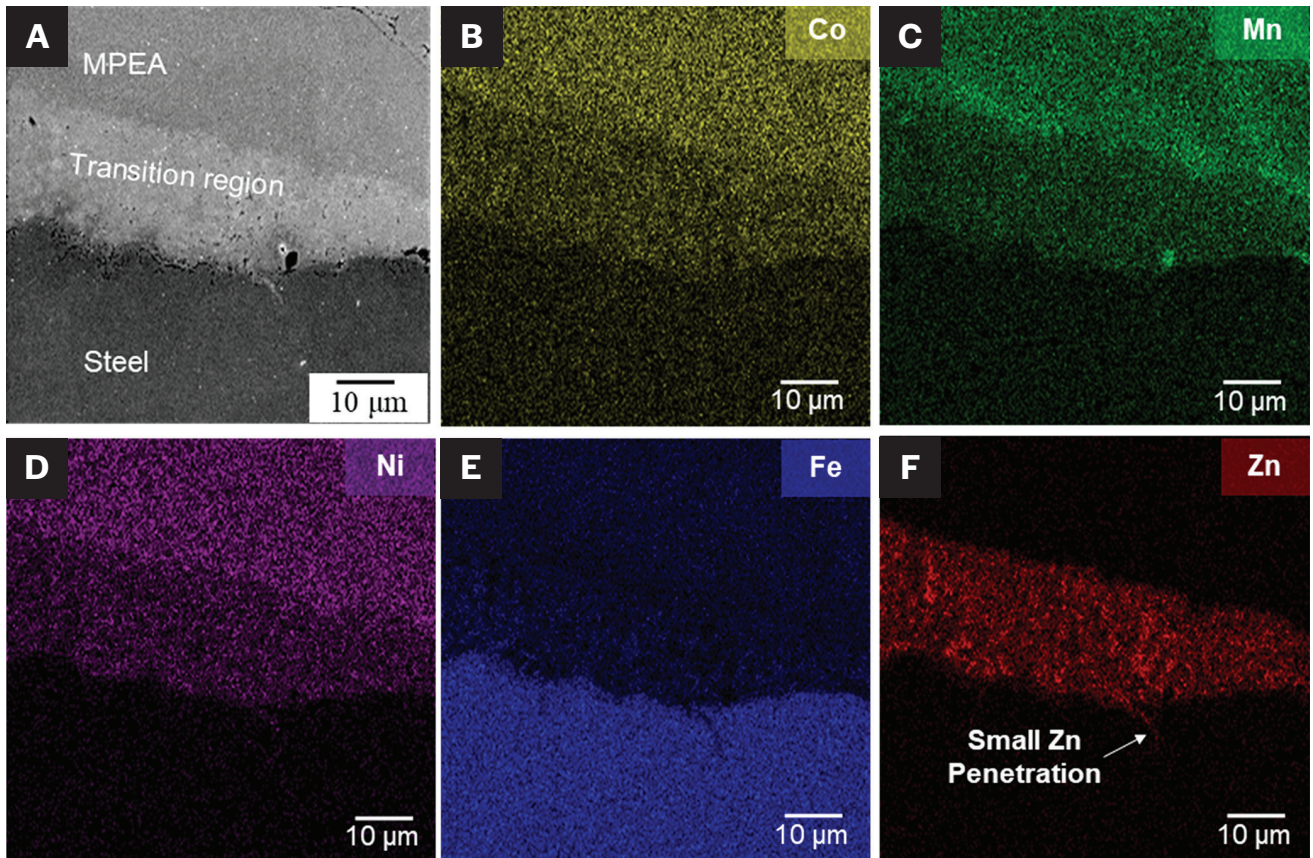


Fig. 10 — A — SEM micrograph; B–F — Co, Mn, Ni, Fe, and Zn EDS maps of the MPEA/steel interface in the more peripheral location of the weld shoulder (location indicated in Fig. 8B).

not vary appreciably with distance from the interface. The strength of the retained austenite peaks also did not vary with distance up to 400 µm from the MPEA/steel interface into the steel side (the full extent of the mapped area in Fig. 4), indicating that the presence of retained austenite was correlated to the RSW thermal history and not influenced by the diffusion of the MPEA elements. No intermetallic phase peaks were detected in the synchrotron XRD patterns across the MPEA/AHSS interface.

Metallurgically, the design objectives of the MPEA foil were to accommodate Zn in a ductile FCC solid solution, minimize the microstructural impact on the steel substrate, and avoid the introduction of any intermetallic phases. The data in Figs. 9–11 demonstrate that each of these was achieved, as Zn was preferentially absorbed, the MPEA was an FCC solid solution, and the DP980 substrate retained its parent composition and microstructure with limited impact by the MPEA.

Tensile-Shear Behavior

Figure 12 compares the tensile-shear behavior of RSW samples with and without the MPEA foils. Figure 12A shows the individual load-displacement curves, and Fig. 12B summarizes and compares the peak load and fracture energy between the two groups of welds. Fracture energy was calculated as the area under the load-displacement curves in Fig. 12A. Figure 12 shows that samples with MPEA foils

exhibited a 21% increase in the mean peak load relative to control samples (31.7 kN vs. 26.2 kN) and an 80% increase in the mean fracture energy (75.6 J vs. 41.9 J). Nugget size assessment on the failed samples revealed that the average nugget diameter increased from 6.96 ± 0.12 mm in the control samples to 7.51 ± 0.06 mm in the experimental samples, an average increase of 7.9%. This increase confirmed that the MPEA foils increased the electrical resistance, resulting in higher welding heat input. As previously discussed, this higher heat input could typically increase the LME susceptibility of the Zn-coated AHSS itself. Still, LME cracks were eliminated from the experimental welds because Zn was effectively accommodated in the solid solution phase of the MPEA in the transition region.

The average peak load increased by 21% in the experimental welds with MPEA foils compared to the control welds. The nugget size increase corresponded to a mean 16.5% increase in the load-bearing area for samples employing MPEA foils, accounting for most of the peak load increase. However, eliminating LME cracks likely contributed to the additional augmentation in load capacity. Another indication of the impact of LME crack elimination by MPEA foils can be manifested by the peak load consistency enhancement. Generally, spot welds can fail via interfacial shear, where the sheets separate along the bond line within the fusion zone, or nugget pull-out, where the fusion zone remains intact and is torn away from one of the welded sheets along its circum-

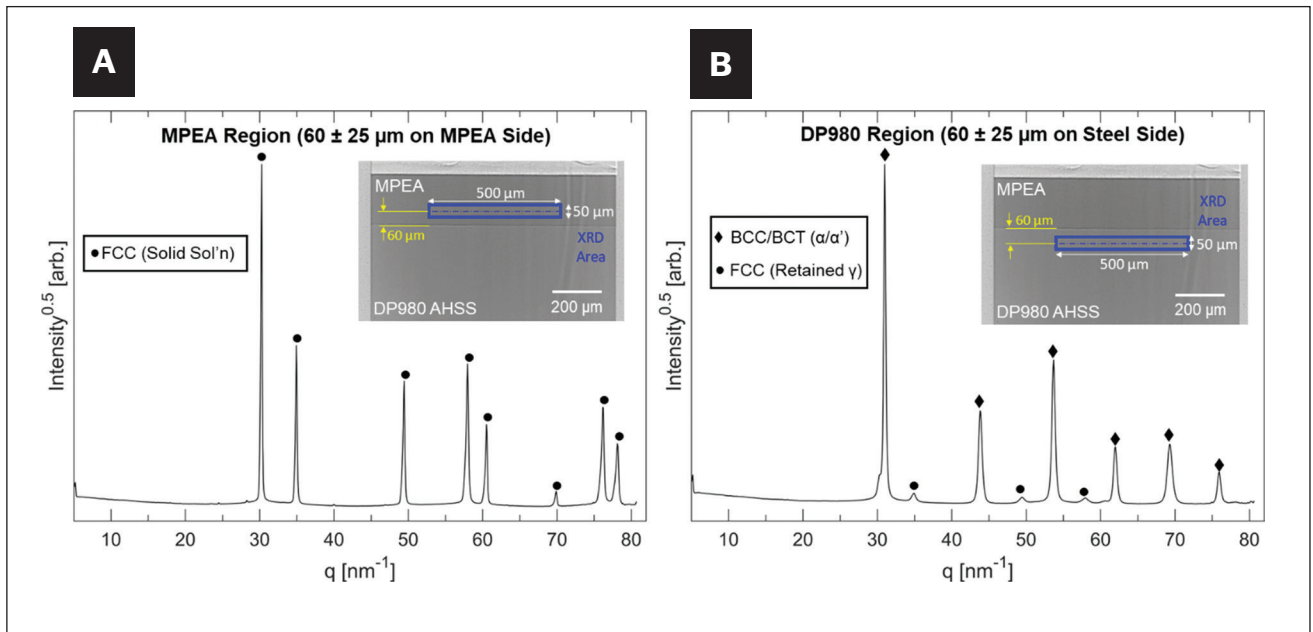


Fig. 11 – Site-specific synchrotron XRD patterns from: A – The MPEA foil region, $60 \pm 25 \mu\text{m}$ away from the foil/substrate interface; B – the DP980 AHSS substrate region, $60 \pm 25 \mu\text{m}$ away from the other side of the interface $60 \mu\text{m}$. The inset x-ray radiographs are annotated to show the diffraction mapping locations.

ference (Refs. 40, 41). In crack-free welds, nugget pull-out is typically correlated with significantly higher fracture energies as it usually requires a high load to be sustained over a larger deformation range to effectuate pull-out (Ref. 41). In cracked welds, shoulder cracks can nucleate premature failure via pull-out (Ref. 42), but the cracks do not govern the failure of samples that fail by interfacial shear.

Table 2 summarizes the failure mode and mechanical properties of individual samples. Among the control samples, the sample that displayed the lowest peak load and fracture energy (Sample C1) failed with pull-out mode, likely a case of LME cracks contributing to premature failure initiating at the weld shoulder. DiGiovanni et al. reported experimental RSW strength deficits due to LME cracks in TRIP 1100 steel ranging from 7.8% to 42.2%, provided that the cracks exceeded a critical length of $300 \mu\text{m}$ when the nugget diameter was 7.3 mm (Ref. 40), similar to the diameter in this work. Although no $300 \mu\text{m}$ cracks were identified in Fig. 6, the sectioning strategy likely could not detect all the cracks in the welds. Consistent with DiGiovanni's finding, Sample C1 displayed a 23% lower peak load than Sample C2, which failed by interfacial shear and, therefore, had cracks that did not govern failure. Sample C3 failed by pull-out mode but at a higher peak load than the interfacial failure and was, thus, likely also a case where cracks did not govern failure. The inconsistency between Samples C1 and C3 indicates that LME cracking occurred with varying severity among control samples, consistent with literature reports on DP980 AHSS (Ref. 3). On the other hand, the two experimental samples that failed by pull-out mode (Sample E2) or in the base material (Sample E3) both exhibited higher peak load than the interfacial failure sample in this group (Sample E1), which was consistent with the crack-free cross-sections observed in Fig. 8.

Future studies are needed to ascertain the role of LME crack elimination via the MPEA foil in mechanical performance. EDS analysis on fracture surfaces would assist in confirming whether control weld failures initiate at LME cracks. A larger test matrix would statistically confirm correlations among LME cracks, failure mode, nugget size, and joint strength discussed above. DP980 is also not as susceptible to LME as Generation 3 AHSS grades, so a more conclusive performance difference could be observed if the MPEA foil strategy was similarly effective at mitigating LME on a more susceptible base material. Further, future studies are needed to determine the technical and economic feasibility and best practices for applying an MPEA foil in an industrial setting and evaluate corrosion and cosmetic impacts in downstream production and service. The MPEA could influence local galvanic corrosion behavior, so the electrode potential of the MPEA should be measured. Cosmetic impacts could likely be kept minimal by reducing the foil thickness to approximately $10 \mu\text{m}$ based on the EDS result in Fig. 9B and using an adhesive to ensure the foil lies flat against the workpiece outside the immediate weld zone.

Conclusions

- Thermodynamic and kinetics calculations predicted that FeMnNiCo MPEA would dissolve Zn during RSW of coated AHSS and form a quinary FeMnNiCoZn MPEA with a single random solid solution FCC phase.

- When $220 \mu\text{m}$ FeMnNiCo MPEA foils were applied to GA DP980 AHSS during RSW, EDS analysis demonstrated that Zn was preferentially dissolved in the MPEA foil after welding. Synchrotron XRD mapping confirmed the sole presence of an FCC solid solution in the MPEA filler and primarily a ferrite/martensite microstructure with some retained austenite

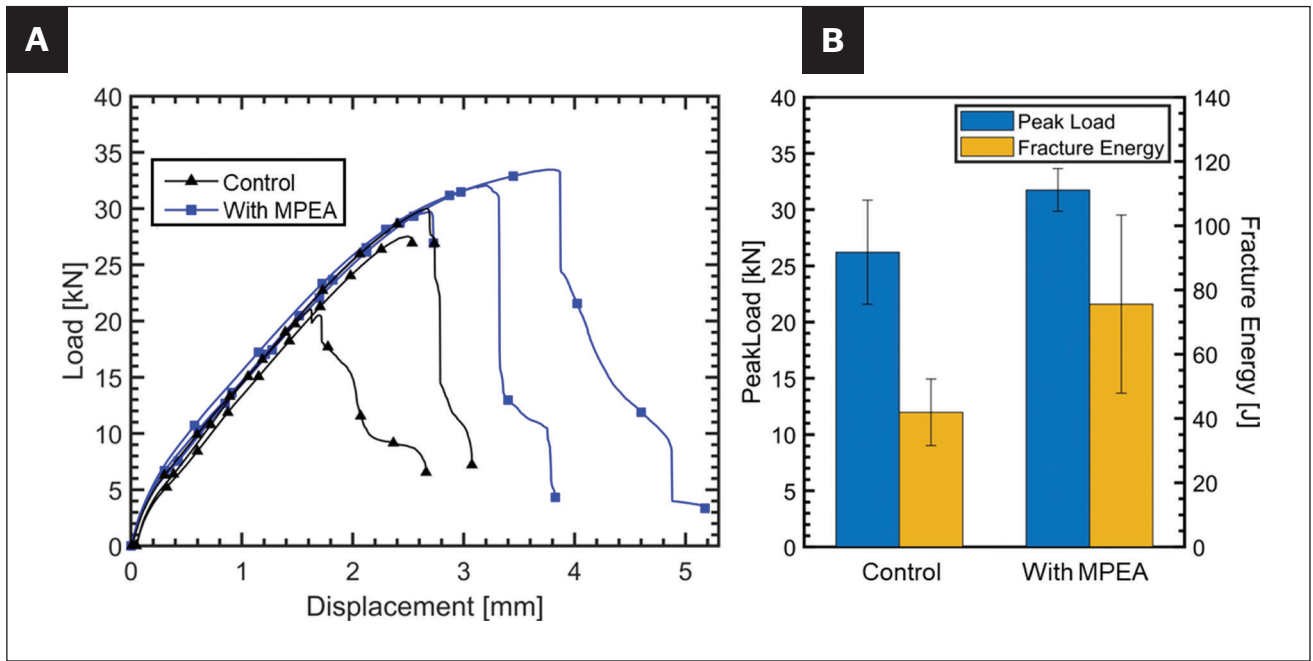


Fig. 12 – Tensile shear test results for samples with and without MPEA foils: A – Load vs. displacement; B – average peak load and fracture energy.

Table 2 – Tensile Shear Testing Results and Failure Mode of All Tested Samples

	Sample #	Peak Load (kN)	Fracture Energy (J)	Failure Mode
Control (without MPEA)	C1	21.1	32.6	Pull-out
	C2	27.5	40.1	Interfacial shear
	C3	30.0	53.0	Pull-out
Experiment (with MPEA)	E1	29.7	49.4	Interfacial shear
	E2	32.1	72.8	Partial pull-out
	E3	33.5	104.6	Base metal

in the AHSS substrate. No intermetallic compounds were detected in the transition region between the MPEA and the steel substrate. The constituent phases agreed with the thermodynamic and kinetic calculations.

- Adding the MPEA foils increased the electrical resistance of the system, leading to a higher welding heat input while using the same welding current. Thus, the nugget diameter increased by 7.9% in experimental samples compared to the control samples welded. Despite the higher heat input, LME was effectively mitigated, as samples employing foils were crack-free, while control samples consistently displayed shoulder cracks.

- Experimental samples displayed a 21% increase in mean peak load and an 80% increase in mean fracture energy over control samples in tensile-shear testing. These mechanical

properties enhancements are attributed to a combination of nugget size increase and elimination of LME cracks in the experimental samples.

Acknowledgments

This work was sponsored by Honda R&D Americas Inc. in Raymond, Ohio, and partially supported by the National Science Foundation under Award No. 1847630. The authors also gratefully acknowledge technical support for DICTRA simulations from Dr. Adam Hope from Thermo-Calc and financial support from the Fulbright foreign student scholarship program. This research used the Advanced Photon Source resources, a U.S Department of Energy (DOE) Office of Science User Facility operated for the DOE Office of Science by

Argonne National Laboratory under Contract No. DE-AC02-06CH11357. Data was collected at Beamline 1-ID-E. Support from Beamline staff is greatly appreciated.

References

1. Ling, Z., Wang, M., and Kong, L. 2018. Liquid metal embrittlement of galvanized steels during industrial processing: A review. *Transactions on Intelligent Welding Manufacturing*: 25–42. DOI: 10.1007/978-981-10-8330-3_2
2. Ashiri, R., Haque, M. A., Ji, C., Shamanian, M., Salimijazi, H. R., and Park, Y. 2015. Supercritical area and critical nugget diameter for liquid metal embrittlement of Zn-coated twinning induced plasticity steels. *Scripta Materialia* 109(12): 6–10. DOI: 10.1016/j.scriptamat.2015.07.006
3. Bhattacharya, D. 2018. Liquid metal embrittlement during resistance spot welding of Zn-coated high-strength steels. *Materials Science and Technology* 15(34): 1809–1829. DOI: 10.1080/02670836.2018.1461595
4. Tolf, E., Hedegård, J., and Melander, A. 2013. Surface breaking cracks in resistance spot welds of dual phase steels with electrogalvanized and hot dip zinc coating. *Science and Technology of Welding and Joining* 1(18): 25–31. DOI: 10.1179/1362171812Y.0000000068
5. Ashiri, R., Shamanian, M., Salimijazi, H. R., Haque, M. A., Bae, J., Ji, C., Chin, K., and Park, Y. 2016. Liquid metal embrittlement-free welds of Zn-coated twinning induced plasticity steels. *Scripta Materialia* 114: 41–47. DOI: 10.1016/j.scriptamat.2015.11.027
6. Bhattacharya, D., et al. 2021. Influence of the starting microstructure of an advanced high strength steel on the characteristics of Zn-assisted liquid metal embrittlement. *Materials Science and Engineering: A* 804. DOI: 10.1016/j.msea.2020.140391
7. Kang, H., Cho, L., Lee, C., and De Cooman, B. C. 2016. Zn penetration in liquid metal embrittled TWIP steel. *Metallurgical and Materials Transactions A* 47: 2885–2905. DOI: 10.1007/s11661-016-3475-x
8. Gordon, P., and An, H. H. 1982. The mechanisms of crack initiation and crack propagation in metal-induced embrittlement of metals. *Metallurgical Transactions A* 13: 457–472. DOI: 10.1007/BF02643354
9. Stoloff, N. S., and Johnson, T. L. 1963. Crack propagation in a liquid metal environment. *Acta Metallurgica* 11(4): 251–256. DOI: 10.1016/0001-6160(63)90180-9
10. De Cooman, B. C. 2016. “High Mn TWIP steel and medium Mn steel.” In *Automotive Steels: Design, Metallurgy, Processing and Applications*, edited by Rana, R., and Singh, S. B., 317–385. Woodhead Publishing. DOI: 10.1016/B978-0-08-100638-2.00011-0
11. Kolman, D. G., and Chavarria, R. 2004. Liquid-metal embrittlement of Type 316L stainless steel by gallium as measured by elastic-plastic fracture mechanics. *Corrosion* 60(3): 254–261. DOI: 10.5006/1.3287729
12. Barthelmie, J., Schram, A., and Wesling, V. 2016. Liquid metal embrittlement in resistance spot welding and hot tensile tests of surface-refined TWIP steels. *IOP Conference Series: Materials Science and Engineering* 118. DOI: 10.1088/1757-899X/118/1/012002
13. Kim, Y. G., Kim, I. J., Kim, J. S., Chung, Y. I., and Choi, D. Y. 2014. Evaluation of surface crack in resistance spot welds of Zn-coated steel. *Materials Transactions* 1(55): 171–175. DOI: 10.2320/matertrans.M2013244
14. He, L. et al. 2019. Suppression of liquid metal embrittlement in resistance spot welding of TRIP steel. *Science and Technology of Welding and Joining* 6(24): 579–586. DOI: 10.1080/13621718.2019.1573011
15. Li, X., Lawson, S., Zhou, Y., and Goodwin, F. 2007. Novel technique for laser lap welding of zinc coated sheet steels. *Journal of Laser Applications* 4(19): 259–264. DOI: 10.2351/1.2795755
16. Yeh, J. W. 2006. Recent progress in high-entropy alloys. *Annales de Chimie Science des Matériaux* 6(31): 633–648.
17. Yeh, J. W. 2013. Alloy design strategies and future trends in high-entropy alloys. *JOM* 65: 1759–1771. DOI: 10.1007/s11837-013-0761-6
18. Miracle, D. B., and Senkov, O. N. 2017. A critical review of high entropy alloys and related concepts. *Acta Materialia* 122: 448–511. DOI: 10.1016/j.actamat.2016.08.081
19. Yeh, J. W. et al. 2004. Nanostructured high-entropy alloys with multiple principal elements: novel alloy design concepts and outcomes. *Advanced Engineering Materials* 5(6): 299–303. DOI: 10.1002/adem.200300567
20. Gao, M., Schneiderman, B., Gilbert, S. M., and Yu, Z. 2019. Microstructural evolution and mechanical properties of nickel-base superalloy brazed joints using a MPCA filler. *Metallurgical and Materials Transactions A* 11(50): 5117–5127. DOI: 10.1007/s11661-019-05386-8
21. Schneiderman, B., DeNonno, O., Klemm-Toole, J., and Yu, Z. 2022. Ductile braze repairs for Ni-base superalloys using novel MPEA filler. *Welding Journal* 3(101): 85-s to 95-s. DOI: 10.29391/2022.101.007
22. Takeuchi, A., and Inoue, A. 2005. Classification of bulk metallic glasses by atomic size difference, heat of mixing and period of constituent elements and its application to characterization of the main alloying element. *Materials Transactions* 12(46): 2817–2829. DOI: 10.2320/matertrans.46.2817
23. Tapia, A. J. S. F., Yim, D., Kim, H. S., and Lee, B. 2018. An approach for screening single phase high-entropy alloys using an in-house thermodynamic database. *Intermetallics* 101(10): 56–63. DOI: 10.1016/j.intermet.2018.07.009
24. Ye, Y. F., Wang, Q., Lu, J., Liu, C. T., and Yang, Y. 2016. High-entropy alloy: challenges and prospects. *Materials Today* 6(19): 349–362. DOI: 10.1016/j.mattod.2015.11.026
25. Murty, B. S., Yeh, J. W., Ranganathan, S., and Bhattacharjee, P. 2019. *High-Entropy Alloys*. Elsevier Science.
26. Zhang, Y., Guo, S., Liu, C. T., and Yang, X. 2016. “Phase formation rules.” In *High-Entropy Alloys*, edited by Gao, M., Yeh, J.-W., Liaw, P., and Zhang, Y., 21–49. Springer. DOI: 10.1007/978-3-319-27013-5_2
27. Murali, M., Babu, S. P. K., Krishna, B. J., and Vallimanalan, A. 2016. Synthesis and characterization of AlCoCrCuFeZn_x high-entropy alloy by mechanical alloying. *Progress in Natural Science: Materials International* 4(26): 380–384. DOI: 10.1016/j.pnsc.2016.06.008
28. Takeuchi, A., and Inoue, A. 2000. Calculations of mixing enthalpy and mismatch entropy for ternary amorphous alloys. *Materials Transactions JIM* 11(41): 1372–1378. DOI: 10.2320/matertrans1989.41.1372
29. de Boer, F. R., Mattens, W. C. M., Boom, R., Miedema, A. R., and Niessen, A. K. 1988. *Cohesion In Metals*. Amsterdam: North-Holland.
30. Hu, J., Walker, E., Yu, Z., Abdelmotagaly, A., and Schneiderman, B. Multi-material component and methods of making thereof. US patent 11318566, filed November 13, 2020, and issued May 3, 2022.
31. Hou, Z. G., Zhao, J., Xu, L. Q., and Guo, Z. 2010. A simplified transient thermal analysis of resistance spot welding process. *Advanced Materials Research* 154–155: 443–446. DOI: 10.4028/www.scientific.net/AMR.154-155.443
32. Schneiderman, B., Hansen, A., Chuang, A. C., and Yu, Z. 2023. Influence of oxygen on performance of multi-principal element alloy as braze filler for Ni-base alloys. *Journal of Manufacturing Processes* 87: 25–35. DOI: 10.1016/j.jmapro.2023.01.017
33. MacDonald, B. E. et al. 2019. Influence of phase decomposition on mechanical behavior of an equiatomic CoCuFeMnNi high entropy alloy. *Acta Materialia* 181: 25–35. DOI: 10.1016/j.actamat.2019.09.030
34. Raelison, R. et al. 2012. Contact conditions on nugget development during resistance spot welding of Zn coated steel sheets using rounded tip electrodes. *Journal of Materials Processing Technology* 212: 1663–1669. DOI: 10.1016/j.jmatprotec.2012.03.009

35. Schneiderman, B., Chuang, A. C., Kenesei, P., and Yu, Z. 2021. In-situ synchrotron diffraction and modeling of non-equilibrium solidification of a MnFeCoNiCu alloy. *Scientific Reports* 11. DOI: 10.1038/s41598-021-85430-z
36. Schneiderman, B., Chuang, A. C., and Yu, Z. 2023. Synchrotron X-ray diffraction analysis of constituent phases in transition joint between nickel alloy 738LC and a MnFeCoNiCu alloy. *Materialia* 32. DOI: 10.1016/j.mtla.2023.101911
37. Baltazar Hernandez, V. H. 2010. Effect of martensite tempering on HAZ-softening and tensile properties of 648 resistance spot welded dual-phase steels. PhD. diss, University of Waterloo, Waterloo, Ontario.
38. Nayak, S. S., Biro, E., and Zhou, Y. 2012. Resistance spot welding of dual-phase steels: Heat affected zone softening and tensile properties. *Trends in Welding Research, Proceedings of the 9th International Conference*.
39. Yan, K., Liss, K. D., Timokhina, I. B., and Pereloma, E. V. 2016. In situ synchrotron X-ray diffraction studies of the effect of microstructure on tensile behavior and retained austenite stability of thermo-mechanically processed transformation induced plasticity steel. *Materials Science and Engineering A* 662:185–197. DOI: 10.1016/j.msea.2016.03.048
40. DiGiovanni, C., Han, X., Powell, A., Biro, E., Zhou, N. Y. 2019. Experimental and numerical analysis of liquid metal embrittlement crack location. *Journal of Materials Engineering and Performance* 28: 2045–2052. DOI: 10.1007/s11665-019-04005-2
41. Chao, Y. J. 2003. Ultimate strength and failure mechanism of resistance spot weld subjected to tensile, shear, or combined tensile/shear loads. *Journal of Engineering Materials and Technology* 125(2): 125–132. DOI: 10.1115/1.1555648
42. DiGiovanni, C., Biro, E., Zhou, N. Y. 2019. Impact of liquid metal embrittlement cracks on resistance spot weld static strength. *Science and Technology of Welding and Joining* 3: 218–224. DOI: 10.1080/13621718.2018.1518363

ABDELRAHMAN ABDELMOTAGALY, BENJAMIN SCHNEIDERMAN, and **ZHENZHEN YU** (*zyu@mines.edu*) are with Colorado School of Mines, Golden, Colo. **JIANXUN HU** is with Honda R&D Americas, Inc., Raymond, Ohio. **ANDREW CHIH PIN CHUANG** is with Advanced Photon Source, Argonne National Laboratory, Lemont, Ill.